RSC Advances

PAPER

View Article Online
View Journal | View Issue

Cite this: *RSC Adv.*, 2021, **11**, 20725

Interfacial charge-transfer transitions in SnO_2 functionalized with benzoic acid derivatives

Jun-ichi Fujisawa * and Minoru Hanaya

Interfacial charge-transfer transitions (ICTTs) between organic compounds and inorganic semiconductors have recently attracted increasing attention for their potential applications in solar energy conversions and chemical sensing due to the unique functions of visible-light absorption with colourless organic molecules and direct charge separation. However, inorganic semiconductors available for ICTT are quite limited to a few kinds of metal-oxide semiconductors (TiO_2, ZnO, *etc.*). Particularly, the exploration of ICTT in inorganic semiconductors with a lower-energy conduction band such as SnO_2 is an important issue for realizing a wide range of visible-light absorption for organic adsorbates with the deep highest occupied molecular orbital (HOMO) such as benzoic acid derivatives. Here, we report the first observation of ICTT in SnO_2. SnO_2 nanoparticles show a broad absorption band in the visible region by chemisorption of 4-dimethylaminobenzoic acid (4-DMABA) and 4-aminobenzoic acid (4-ABA)) *via* the carboxylate group. The wavelength range of the ICTT band significantly changes depending on the kind of substituent group. The ionization potential measurement and density functional theory (DFT) analysis reveal that the absorption band is attributed to ICTT from the HOMO of the adsorbed benzoic acid derivatives to the conduction band of SnO_2. In addition, we clarify the mechanism of ICTT in SnO_2 computationally. Our research opens up a way to the fundamental research on ICTT in SnO_2 and applications in solar energy conversions and chemical sensing.

Received 1st May 2021
Accepted 3rd June 2021

DOI: 10.1039/d1ra03422g

rsc.li/rsc-advances

Introduction

Organic–inorganic hybrid nanomaterials hold great promise for developing new functional materials. Surface coordination complexes of inorganic semiconductor nanomaterials such as TiO_2 nanoparticles with organic compounds characteristically show interfacial charge-transfer transitions across organic–inorganic interfaces, which enable the absorption of visible light with colourless organic compounds and direct photoinduced charge separation, as shown in Fig. 1(a).[1–16] Due to these key features, ICTT have recently attracted increasing interest because of their potential applications in solar energy conversions such as photovoltaic conversion[10,17,18] and photocatalysis[19–29] and chemical sensing (direct visualization,[2,3,30–33] surface enhanced Raman scattering (SERS),[34,35] and visible-light circular dichroism (CD)[36]). So far, ICTT has been studied in TiO_2 nanoparticles chemisorbed with various organic compounds (phenol, catechol, benzenedithiol, aromatic carboxylic acids, aromatic amines, *etc.*), as shown in Fig. 1(b). However, inorganic semiconductors available for ICTT are quite limited to a few kinds of wide band-gap semiconductors (TiO_2, $SrTiO_3$, $BaTiO_3$, ZnO).[37–40] Particularly, the exploration of ICTT in inorganic semiconductors with a lower-energy conduction band such as SnO_2 is a high-priority issue to realize the absorption of visible light with organic adsorbates possessing the deep highest occupied molecular orbital (HOMO) such as benzoic acid derivatives. In addition, SnO_2 is an important semiconductor for electronic and optoelectronic devices and chemical sensors due to the high electron mobility.[41] For these reasons, the observation of ICTT in SnO_2 is a crucial issue for

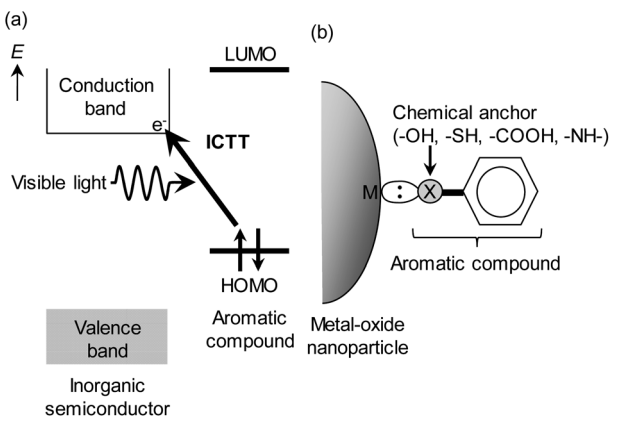

Fig. 1 (a) Schematic energy level diagram of interfacial charge-transfer transitions (ICTTs) between organic compounds and inorganic semiconductors and (b) representative system of surface coordination complexes for ICTT.

Graduate School of Science and Technology, Gunma University, 1-5-1 Tenjin-cho, Kiryu, Gunma, 376-8515, Japan. E-mail: jfujisawa@gunma-u.ac.jp

the fundamental research and applications of ICTT. To our best knowledge, however, there are no reports on ICTT in SnO_2. Here, we report the first observation of ICTT in SnO_2 nanoparticles adsrobed with benzoic acid derivatives, 4-dimethylaminobenzoic acid (4-DMABA) and 4-aminobenozic acid (4-ABA), which have a strong electron-donating group.

Experimental

SnO_2 nanoparticles adsorbed with 4-DMABA were prepared by immersing crystalline SnO_2 nanoparticles (Wako Pure Chemical Industries) with an average particle size of *ca.* 30 nm and a tetragonal crystal structure into the acetonitrile solution of 10 mM 4-DMABA (Tokyo Chemical Industry) for 24 hours at room temperature, filtering and washing well SnO_2 nanoparticles with acetonitrile to remove unadsorbed 4-DMABA, and then vacuum-drying them. SnO_2 nanoparticles adsorbed with 4-ABA were prepared in a similar way with 4-ABA (Tokyo Chemical Industry). The adsorption densities of 4-DMABA and 4-ABA were estimated to be *ca.* 0.20 and 0.22 mmol g^{-1}, respectively, by elementary analysis. Diffuse reflectance spectra were measured by means of a UV-VIS-NIR spectrophotometer (V-670, JASCO). The measured diffuse reflectance (R_{diff}) spectra were converted to the spectra of Kubelka–Munk (KM) function that is defined as the ratio (K/S) of the absorption coefficient (K) to the scattering coefficient (S) by using the following equation, KM function $= (1 - R_{diff})^2/(2R_{diff})$. FT-IR spectra were measured by means of an FT-IR spectrometer (iS10, Nicolet) with a diamond ATR crystal. SnO_2 nanoparticles for IR measurements were prepared *via* immersion in acetonitrile. Photoelectron yield measurements were performed by means of an ionization energy measurement system (BIP-KV201, Bunkoukeiki).

Computational details

For DFT analysis, we built a SnO_2-cluster based model complex $[Sn_9O_{12}H_4(OH)_{15}–OOC–Bz–N(CH_3)_2]$ and $[Sn_9O_{12}H_4(OH)_{15}–OOC–Bz–NH_2]$ (total charge: 0) using the reported X-ray crystallographic data of bulk tetragonal SnO_2 crystals. Structural optimization of the model complexes was performed with the B3LYP functional and def2-TZVP basis set.[42,43] During the geometrical optimization, the Cartesian coordinates of tin and oxygen atoms in the SnO_2 nanocluster were frozen to maintain the crystal structure, while all other atoms (carbon, hydrogen, nitrogen, and oxygen atoms in the adsorbed 4-DMBABA and 4-ABA and hydrogen atoms in the surface hydroxy groups) were relaxed. The vibrational spectrum was calculated with the same functional and basis set. The electronic excitation spectrum was calculated at the same level of theory. All the calculations were performed by using a Gaussian 09 software.[44]

Results and discussion

Crystalline SnO_2 nanoparticles (average size: *ca.* 30 nm) were coloured dark orange by immersion in the acetonitrile solution of 4-DMABA (10 mM). As shown in Fig. 2, SnO_2 nanoparticles treated with 4-DMABA showed a broad absorption band in the visible region with an absorption onset at *ca.* 700 nm, in contrast to the inter-band absorption of SnO_2 ($E_g = 3.6$ eV)[41] and intra-molecular absorption of 4-DMABA in the UV region. For comparison, we measured the Kubelka–Munk spectrum of SnO_2 nanoparticles immersed in the acetonitrile solution of 4-ABA (10 mM). 4-ABA-treated SnO_2 nanoparticles showed a broad absorption band in a narrower visible range with an absorption onset around 600 nm. This result clearly indicates that the wavelength range of the absorption band depends on the kind of substituent group introduced in the benzoic acid derivatives with the red-shift of the absorption onset from *ca.* 600 (4-ABA) to *ca.* 700 nm (4-DMABA) by 0.30 eV. On the other hand, we observed that a weak and broad absorption band appeared in the visible region by only immersion into acetonitrile solvent, as shown by the black solid curve in Fig. 2. This absorption band is presumably related to intra-gap surface levels in the solvent-treated SnO_2 nanoparticles. Although the detail of the electronic transitions remains unknown, this solvent-induced absorption band prevented us from observing ICTT in SnO_2 with other benzoic acid derivatives. By introducing the strong electron-donating groups ($–N(CH_3)_2$ and $–NH_2$) into benzoic acid, we could observe new absorption bands at the longer wavelengths than the solvent-induced absorption.

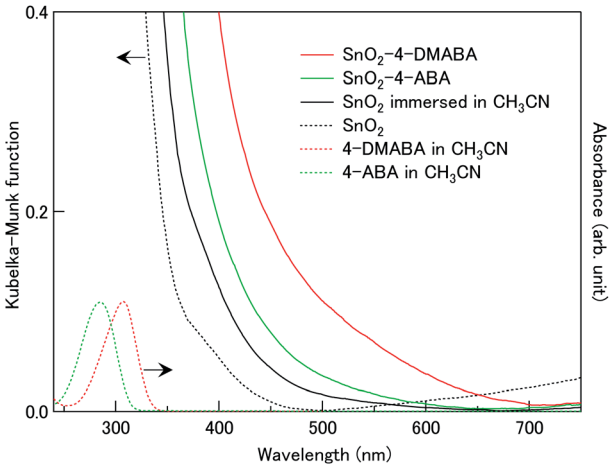

Fig. 2 Kubelka–Munk function spectra of SnO_2 nanoparticles adsorbed with 4-DMABA (red solid curve) and 4-ABA (green solid curve) along with those of SnO_2 nanoparticles with (black dashed curve) and without immersion in acetonitrile (black solid curve) and UV-visible absorption spectra of 4-DMABA (red dashed curve) and 4-ABA (green dashed curve) in acetonitrile.

Fig. 3(a) and (c) show the FT-IR spectra of SnO_2 nanoparticles adsorbed with and without 4-DMABA and that of 4-DMABA, respectively. The SnO_2–4-DMABA complex showed several intramolecular vibrational peaks of the adsorbed 4-DMABA at 1194 (strong), 1356 (strong and broad), 1392 (weak), 1483 (weak), 1520 (weak), and 1607 cm^{-1} (strong). By comparison to the FT-IR spectrum of free 4-DMABA, it is seen that the vibrational mode of the carboxy group at 1660 cm^{-1} disappeared and the strong and broad vibrational peak assigned to the carboxylate group ($–COO^-$) appeared at 1356 cm^{-1} upon adsorption on SnO_2. This result indicates that 4-DMABA chemisorbs on the

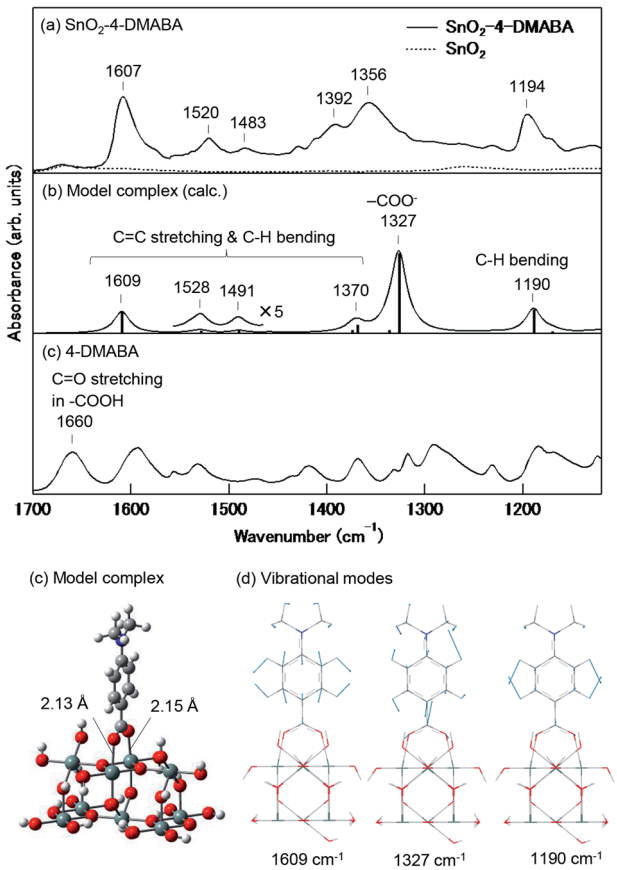

Fig. 3 FT-IR spectra of (a) SnO_2 nanoparticles adsorbed with and without 4-DMABA, (b) calculated IR vibrational spectrum (full width at half maximum: 20 cm^{-1}) of $[Sn_9O_{12}H_4(OH)_{15}–OOC–Bz–N(CH_3)_2]$, and (c) FT-IR spectrum of 4-DMABA. (d) Optimized structure of the model complex and (e) calculated vibrational modes with displacement vectors (water blue) at 1190, 1327, 1609 cm^{-1}. The calculated vibrational wavenumbers are corrected with a scaling factor of 0.975.

SnO_2 surface *via* the carboxylate group though the dehydration condensation reaction of the carboxy group with a surface hydroxy group. In order to confirm this assignment, we analyzed the vibrational structure with density functional theory (DFT) calculations using a model complex $[Sn_9O_{12}H_4(OH)_{15}–OOC–Bz–N(CH_3)_2]$. Fig. 3(d) shows the DFT-optimized structure of the model complex. The $Sn–O_{bridge}$ bond lengths are estimated to be 2.13 and 2.15 Å. The calculated vibrational spectrum of the model complex exhibits intramolecular vibrational peaks of the adsorbed 4-DMABA at 1190 (strong), 1327 (very strong), 1370 (weak), 1491 (weak), 1528 (weak), and 1609 cm^{-1} (strong), which well correspond to the observed vibrational peaks, as shown in Fig. 3(b). Fig. 3(e) shows dominant vibrational modes at 1190, 1327, and 1609 cm^{-1}. As the vibrational mode at 1327 cm^{-1} includes displacement vectors on the carboxylate anchor in contrast to the other vibrations, the vibrational frequency is sensitive to the surface state, which results in inhomogeneous broadening of the vibrational peak. This is the reason why the vibrational peak at 1356 cm^{-1} is broader than the others and the observed relative intensity is much lower than the calculated one. Therefore, the DFT calculation well reproduces the vibrational structure of the SnO_2–4-DMABA surface complex, supporting the chemisorption of 4-DMABA *via* the carboxylate group.

Fig. 4(a) shows photoelectron yield spectra of SnO_2 nanoparticles adsorbed with and without 4-DMABA. SnO_2 nanoparticles showed photoelectrons at photon energies higher than *ca.* 7.9 eV, which are assigned to the valence-band electrons. Accordingly, the ionization potential of SnO_2 nanoparticles is estimated to be *ca.* 7.9 eV. By contrast, SnO_2 nanoparticles adsorbed with 4-DMABA showed photoelectrons at much lower photon energies with an onset energy at *ca.* 6.0 eV. This photoelectron signal is attributable to electrons in HOMO of the adsorbed 4-DMABA. In order to confirm this assignment, we calculated total and partial densities-of-states (DOSs) of the model complex. As shown in Fig. 5(a), the HOMO of the adsorbed 4-DMABA lies within the band gap of the SnO_2 nanocluster, which indicates that the photoelectron signal is assigned to the HOMO level of the adsorbed 4-DMABA. Note that the calculated HOMO energy (−6.90 eV) is lower than the ionization potential. This difference might be due to the negative surface charge of SnO_2 nanoparticles, as reported in the previous literature.[45] The negative surface charge elevates the HOMO level of the adsorbed 4-DMABA *via* coulombic interactions.

Based on the estimated ionization potentials, the energy level diagram of the SnO_2–4-DMABA surface complex is depicted, as shown in Fig. 4(b). The energy of the conduction-band bottom of

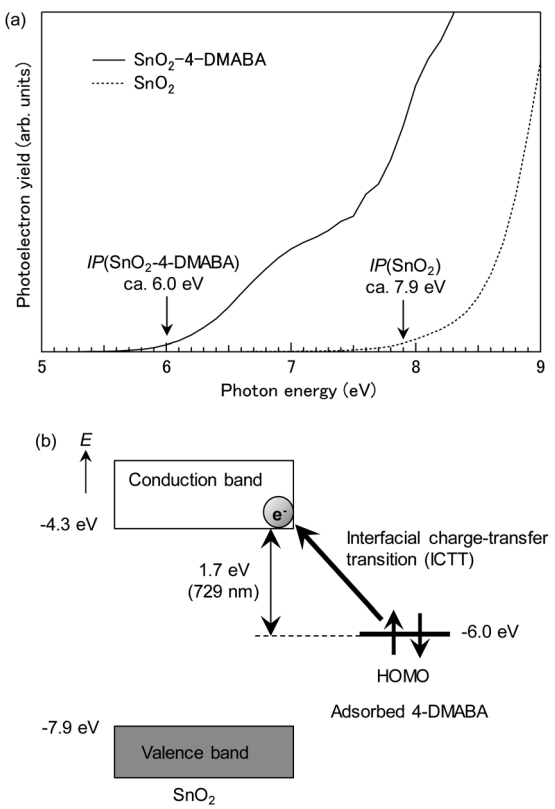

Fig. 4 (a) Photoelectron yield spectra of SnO_2 nanoparticles adsorbed with and without 4-DMABA and (b) energy level diagram of the SnO_2–4-DMABA surface complex.

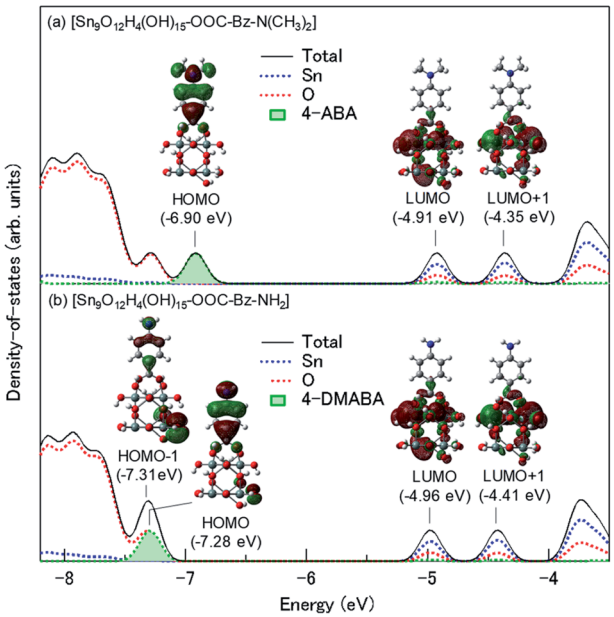

Fig. 5 Total and partial densities-of-states (full width at half maximum: 0.2 eV) of (a) $[Sn_9O_{12}H_4(OH)_{15}–OOC–Bz–N(CH_3)_2]$ and (b) $[Sn_9O_{12}H_4(OH)_{15}–OOC–Bz–NH_2]$ along with isosurface plots ($|isovalue| = 0.02a_0^{-3/2}$) of HOMO, LUMO and LUMO+1 in (a) and HOMO−1, HOMO, LUMO, and LUMO+1 in (b).

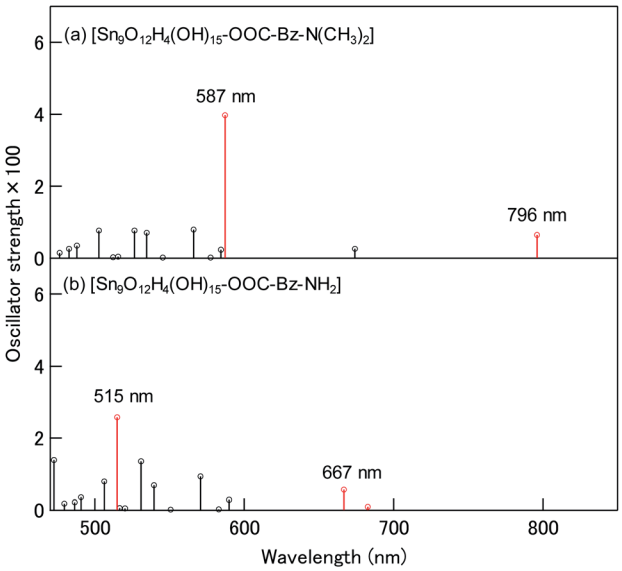

Fig. 6 Calculated electronic excitation spectra of (a) $[Sn_9O_{12}H_4(OH)_{15}–OOC–Bz–N(CH_3)_2]$ and (b) $[Sn_9O_{12}H_4(OH)_{15}–OOC–Bz–NH_2]$. ICTTs are shown red.

SnO_2 is estimated to be −4.3 eV *vs.* vacuum level from the reported band gap (E_g = *ca.* 3.6 eV).[41] The estimated conduction-band edge is lower by 0.25 eV than that (−4.05 eV)[46] of anatase TiO_2, which is consistent with the reported result in the literature.[47] The energy difference of 1.7 eV between the conduction-band bottom of SnO_2 and HOMO of the adsorbed 4-DMABA approximately agrees with the onset energy (1.77 eV) of the broad absorption band of the SnO_2–4-DMABA complex. This result indicates that the absorption band is attributed to ICTT from the HOMO of the adsorbed 4-DMABA to the conduction band of SnO_2 nanoparticles.

Fig. 6(a) shows the electronic excitation spectrum of the model complex calculated by time-dependent DFT (TD-DFT) calculations. The model complex shows relatively strong electronic excitation at 796 and 587 nm in the visible region. These excitations are assigned to the HOMO → LUMO and HOMO → LUMO+1 electronic transitions, respectively, as shown in Table 1. LUMO+1 denotes the second lowest unoccupied molecular orbital. The LUMO and LUMO+1 correspond to the conduction band of SnO_2, as shown in Fig. 5(a). Therefore, these excitations are attributed to ICTTs from the HOMO of the adsorbed 4-DMABA to the conduction band of SnO_2, supporting the above-mentioned ICTT assignment. As shown by the isosurface plots in the inset of Fig. 5(a), the LUMO and LUMO+1 are significantly delocalized on the carboxylate anchor moiety of the adsorbed 4-DMABA. The delocalization of the unoccupied orbitals on the carboxylate group increases the transition dipole moments of ICTTs in SnO_2. This is the main mechanism for ICTT in the SnO_2 surface coordination complexes with the benzoic acid derivatives.

Fig. 6(b) shows the electronic excitation spectrum of the model complex with 4-ABA, $[Sn_9O_{12}H_4(OH)_{15}–OOC–Bz–NH_2]$. The model complex shows two dominant ICTT excitations at 667 and 515 nm. The lower energy ICTT is the mixed electronic excitation of HOMO → LUMO and HOMO−1 → LUMO and the higher energy ICTT is the mixed electronic excitation of HOMO → LUMO+1 and HOMO−1 → LUMO+1. HOMO−1 denotes the second highest occupied molecular orbital. Fig. 5(b) indicates that the HOMO at −7.28 eV in the SnO_2–4-ABA model complex is predominantly distributed on the adsorbed molecule (87%) with weak delocalization on surface hydroxy groups. In contrast, the HOMO−1 at −7.31 eV is mainly distributed on surface hydroxy groups and slightly delocalized onto the adsorbate (12%). Therefore, these excitations have ICTT character. The lower energy ICTT red-shifts from 667 (4-ABA) to 796 nm (4-DMABA) by 0.30 eV and the higher energy ICTT red-shifts from 515 (4-ABA) to 587 nm (4-DMABA) by 0.30 eV. This calculation result quantitatively agrees with the above-mentioned experimental result of the red-shift (0.30 eV) of the ICTT band by changing the substituent group from the amino group to dimethylamino group. Thus, the red-shift originates from the increase in the HOMO energy from −7.28 (4-ABA) to −6.90 eV (4-ABA), as shown in Fig. 5.

Table 1 Wavelength (λ), oscillator strength (f), and electronic configuration of dominant interfacial charge-transfer excitations calculated for $[Sn_9O_{12}H_4(OH)_{15}–OOC–Bz–N(CH_3)_2]$ and $[Sn_9O_{12}H_4(OH)_{15}–OOC–Bz–NH_2]$

Adsorbate	λ (nm)	f	Electronic configuration
4-DMABA	587	0.0398	HOMO → LUMO+1 (98%)
	796	0.0065	HOMO → LUMO (99%)
4-ABA	515	0.0258	HOMO → LUMO+1 (67%)
			HOMO−1 → LUMO+1 (31%)
	667	0.0057	HOMO → LUMO (52%)
			HOMO−1 → LUMO (47%)

Conclusion

In summary, we demonstrated ICTT in SnO_2 nanoparticles for the first time. SnO_2 nanoparticles show a broad ICTT band in the visible region upon chemisorption of 4-DMABA and 4-ABA *via* the carboxylate group. The wavelength range of ICTT absorption significantly changes depending on the kind of substituent group in the benzoic acid derivatives. We can control the ICTT absorption range by adjusting the electron-donating ability of substituent group. Our research opens up a way to the fundamental research of ICTT in SnO_2 and its wide applications in solar energy conversions and chemical sensing.

Conflicts of interest

There are no conflicts to declare.

Acknowledgements

We thank Mr T. Amano and Mr K. Nakajima of Bunkoukeiki for their kind cooperation in photoelectron yield measurements. The elementary analysis was performed using the instrument at the Center for Instrumental Analysis of Gunma University.

Notes and references

1 J. Moser, S. Punchihewa, P. P. Infelta and M. Grätzel, *Langmuir*, 1991, **7**, 3012.
2 T. Rajh, J. M. Nedeljkovic, L. X. Chen, O. Poluektov and M. C. Thurnauer, *J. Phys. Chem. B*, 1999, **103**, 3515.
3 T. Rajh, L. X. Chen, K. Lukas, T. Liu, M. C. Thurnauer and D. M. Tiede, *J. Phys. Chem. B*, 2002, **106**, 10543.
4 J. Fujisawa, S. Matsumura and M. Hanaya, *Chem. Phys. Lett.*, 2016, **657**, 172.
5 J. Fujisawa, T. Eda, G. Giorgi and M. Hanaya, *J. Phys. Chem. C*, 2017, **121**, 18710.
6 D. N. Sredojević, T. Kovač, E. Džunuzović, V. Đorđević, B. N. Grgur and J. M. Nedeljković, *Chem. Phys. Lett.*, 2017, **686**, 167.
7 J. Fujisawa, R. Muroga and M. Hanaya, *Phys. Chem. Chem. Phys.*, 2015, **17**, 29867.
8 J. Fujisawa, R. Muroga and M. Hanaya, *Phys. Chem. Chem. Phys.*, 2016, **18**, 22286.
9 A. G. Thomas, M. J. Jackman, M. Wagstaffe, H. Radtke, K. Syres, J. Adell, A. Lévy and N. Martsinovich, *Langmuir*, 2014, **30**, 12306.
10 J. Fujisawa and M. Nagata, *Chem. Phys. Lett.*, 2015, **619**, 180.
11 S. Manzhos and K. Kotsis, *Chem. Phys. Lett.*, 2016, **660**, 69.
12 J. Fujisawa and M. Hanaya, *J. Phys. Chem. C*, 2018, **122**, 8.
13 M. Bledowski, L. Wang, A. Ramakrishnan, O. V. Khavryuchenko, V. D. Khavryuchenko, P. C. Ricci, J. Strunk, T. Cremer, C. Kolbeck and R. Beranek, *Phys. Chem. Chem. Phys.*, 2011, **13**, 21511.
14 J. Fujisawa, *Chem. Phys. Lett.*, 2020, **739**, 136974.
15 R. Jono, J. Fujisawa, H. Segawa and K. Yamashita, *J. Phys. Chem. Lett.*, 2011, **2**, 1167.
16 S. Manzhos, R. Jono, K. Yamashita, J. Fujisawa, M. Nagata and H. Segawa, *J. Phys. Chem. C*, 2011, **115**, 21487.
17 J. Fujisawa, *Phys. Chem. Chem. Phys.*, 2015, **17**, 12228.
18 J. Fujisawa, *Energies*, 2020, **13**, 2521.
19 V. H. Houlding and M. Grätzel, *J. Am. Chem. Soc.*, 1983, **105**, 5695.
20 S. Ikeda, C. Abe, T. Torimoto and B. Ohtani, *J. Photochem. Photobiol., A*, 2003, **160**, 61.
21 E. A. Rozhkova, I. Ulasov, B. Lai, N. M. Dimitrijevic, M. S. Lesniak and T. Rajh, *Nano Lett.*, 2009, **9**, 3337.
22 N. M. Dimitrijevic, E. Rozhkova and T. Rajh, *J. Am. Chem. Soc.*, 2009, **131**, 2893.
23 G. Zhang and W. Choi, *Chem. Commun.*, 2012, **48**, 10621.
24 T. Kamegawa, H. Seto, S. Matsuura and H. Yamashita, *ACS Appl. Mater. Interfaces*, 2012, **4**, 6635.
25 M. Bledowski, L. Wang, A. Ramakrishnan, A. Bétard, O. V. Khavryuchenko and R. Beranek, *ChemPhysChem*, 2012, **13**, 3018.
26 S. P. Pitre, T. P. Yoon and J. C. Scaiano, *Chem. Commun.*, 2017, **53**, 4335.
27 K. L. Orchard, D. Hojo, K. P. Sokol, M.-J. Chan, N. Asao, T. Adschiri and E. Reisner, *Chem. Commun.*, 2017, **53**, 12638.
28 J.-L. Shi, H. Hao, X. Li and X. Lang, *Catal. Sci. Technol.*, 2018, **8**, 3910.
29 J.-L. Shi, H. Hao and X. Lang, *Sustainable Energy Fuels*, 2019, **3**, 488.
30 J. Fujisawa, N. Kikuchi and M. Hanaya, *Chem. Phys. Lett.*, 2016, **664**, 178.
31 J. Fujisawa, S. Matsumura and M. Hanaya, *ChemistrySelect*, 2016, **1**, 5590.
32 J. Fujisawa, T. Eda and M. Hanaya, *Chem. Phys. Lett.*, 2017, **684**, 328.
33 J. Fujisawa, S. Matsumura and M. Hanaya, *ChemistrySelect*, 2017, **2**, 6097.
34 A. Musumeci, D. Gosztola, T. Schiller, N. M. Dimitrijevic, V. Mujica, D. Martin and T. Rajh, *J. Am. Chem. Soc.*, 2009, **131**, 6040.
35 S. J. Hurst, H. C. Fry, D. J. Gosztola and T. Rajh, *J. Phys. Chem. C*, 2011, **115**, 620.
36 J. Fujisawa, N. Kaneko, T. Eda and M. Hanaya, *Chem. Commun.*, 2018, **54**, 8490.
37 J. Fujisawa, T. Eda and M. Hanaya, *J. Phys. Chem. C*, 2016, **120**, 21162.
38 T. Eda, J. Fujisawa and M. Hanaya, *J. Phys. Chem. C*, 2018, **122**, 16216.
39 J. Fujisawa, N. Kaneko and M. Hanaya, *Chem. Commun.*, 2020, **56**, 4090.
40 J. Fujisawa, *Chem. Phys. Lett.*, 2021, **778**, 138774.
41 M. Batzill and U. Diebold, *Prog. Surf. Sci.*, 2005, **79**, 47.
42 F. Weigend and R. Ahlrichs, *Phys. Chem. Chem. Phys.*, 2005, **7**, 3297.
43 F. Weigend, *Phys. Chem. Chem. Phys.*, 2006, **8**, 1057.
44 M. J. Frisch, *Gaussian 09, revision D.01*, Gaussian Inc, Wallingford, CT, 2009.
45 X. Li, Q. Yu, C. Yu, Y. Huang, R. Li, J. Wang, F. Guo, Y. Zhang, S. Gao and L. Zhao, *J. Mater. Chem. A*, 2015, **3**, 8076.
46 J. Fujisawa, T. Eda and M. Hanaya, *Chem. Phys. Lett.*, 2017, **685**, 23.
47 J. M. Bolts and M. S. Wrighton, *J. Phys. Chem.*, 1976, **80**, 2641.